AIAA JOURNAL
Vol. 36, No. 2, February 1998

Global Far-Field Computational Boundary Conditions for C- and O-Grid Topologies

A. Verhoff*
McDonnell Douglas Corporation, Saint Louis, Missouri 63166

Global far-field computational boundary conditions for inviscid external flow problems have been developed for C- and O-grid topologies. This analysis represents a unified approach for two-dimensional external flow problems. These boundary conditions are derived from analytic solutions of an asymptotic form of the steady-state Euler equations and have improved accuracy compared to characteristic boundary conditions commonly used in practice. The Euler equations are asymptotically linearized about a constant pressure, rectilinear flow condition, which is the true boundary condition at infinity. Previous work had developed higher-order boundary conditions for C-grid topologies by assuming small perturbations in both pressure and flow direction at and beyond the computational boundary, by decoupling the inflow and outflow analyses, and by linearizing the thermodynamic relations. This work lifts these restrictions, although some higher-order compressibility effects are neglected. It is based on a global mapping of the boundary and solution of the resulting Dirichlet–Neumann problem. Because the Euler equations are used to develop the boundary conditions, the flow crossing the boundary can be rotational. The boundary conditions can be used with any numerical Euler solution method and allow computational boundaries to be located very close to the nonlinear region of interest. This leads to a significant reduction in the number of grid points required for numerical solution. Numerical results are presented that show that the boundary conditions and far-field analytic solutions provide a smooth transition across a computational boundary to the true far-field conditions at infinity. They also demonstrate the synergism that can be realized from coupling analytic and computational methods.

Introduction

NUMERICAL solution procedures for nonlinear fluid dynamic equations usually use one or more artificial computational boundaries located at some distance from the primary region of interest to limit the physical domain to finite size. If the flow crossing such a boundary (either inflow or outflow) is subsonic, then some type of computational boundary conditions must be imposed to simulate the influence of the true far-field conditions at infinity, i.e., constant pressure, rectilinear flow. These boundary conditions must be such that waves crossing the boundary do not produce erroneous reflections back into the computational field to degrade the calculations. It is generally acknowledged that it is inappropriate to simply impose freestream conditions (or conditions at infinity) at computational boundaries because of the spurious reflections that are produced. Standard practice has consisted of locating the boundaries quite far from the region of interest in an attempt to simplify the boundary condition models and minimize any effects of inconsistent modeling. The net effect is a significant increase in the number of grid points required for an accurate flowfield calculation.

Boundary modeling procedures for two-dimensional internal flows and external flows utilizing C-grid topologies that allow the computational boundaries to be located much closer to the nonlinear region of interest were presented in Refs. 1 and 2. An upgraded approach is presented that also applies to O-grid topologies. The approaches are limited to steady, inviscid flow, although the flow can be rotational. They represent a logical higher-order extension of the so-called characteristic (or zero-order) boundary conditions applied at each boundary point independently that are commonly used with inviscid or viscous numerical solution methods. They also illustrate a consistent procedure for coupling analytic solutions with nonlinear numerical solutions by means of computational boundary conditions.

Use of local zero-order boundary conditions for internal or external flow problems requires that the computational boundaries be located far from the nonlinear near-field region. Close placement of the boundaries may result in a significant amount of solution degradation. In the analysis presented, the iterative solution method and the linearization of the thermodynamic relations employed in Ref. 2 have been eliminated. The procedure is derived from the Euler equations and is, therefore, applicable to flows having strong entropy producing effects, e.g., shock waves, within the computational region. Such effects can produce large variations in density and Mach number in the far field in the direction normal to streamlines, i.e., an entropy wake, that persist to infinity and that cannot be treated as small perturbations. A potential flow model, e.g., vortex correction due to lift, of such a far field having a vorticity wake is inappropriate because its perturbations decay to zero at infinity.

Many boundary condition models have been proposed in the literature during the past two decades, and a number of the more prominent works are cited herein.[3–8] The most noteworthy models are the nonreflecting boundary conditions that strive to suppress erroneous reflections from the boundary back into the computational domain by eliminating all incoming waves. The assumption that nothing occurs beyond the boundary that propagates any meaningful information toward the computational domain is questionable unless the boundary is far removed and is incorrect if the flow is rotational. The models are typically derived by linearizing the steady or unsteady fluid dynamic equations (usually Euler) about constant far-field conditions and solving the resulting system assuming a generalized waveform. However, their utility is compromised if strong rotational effects are produced within the computational domain because flow variables other than pressure and flow angle are not constant in the far field if the flow is treated as inviscid. In that case, linearization in terms of primitive or conservative variables yields perturbation quantities that do not vanish at infinity. Moreover, linearization about average far-field conditions becomes questionable if rotational effects are strong. It was shown earlier that conditions are achieved readily for internal flows where a shock wave produces far-field Mach numbers downstream that vary by a factor of two.[9] Streamline-normal gradient variations can be even more pronounced, which cause strong interactions to persist in the far field. It was also shown previously that a linearization with decaying perturbations is possible,[2,9] but the linear equation system has nonconstant coefficients. The present analysis leads to a linear constant coefficient equation system, which is a significantly simpler and more accurate model of the far field.

Received March 23, 1996; revision received July 21, 1997; accepted for publication Sept. 9, 1997.

*MDC Research Fellow, Computational Fluid Dynamics, P.O. Box 516, MC 1067126. Associate Fellow AIAA.

The present analysis starts from a two-dimensional Euler description in physical space with velocity and flow angle as dependent variables. The equations are rewritten in a linear form derived from the asymptotic far-field behavior wherein pressure is constant and streamlines are rectilinear (true conditions at infinity). The asymptotic analysis allows rotational effects to be taken into account by a change in dependent variable and eliminates the need to linearize the thermodynamic relations. Higher-order compressibility effects that vanish at infinity are treated as right-hand-side (RHS) source terms, which are neglected in the far-field analysis. These simplified equations are assumed applicable in the far-field region beyond a computational boundary. This improved asymptotic Euler model can be applied to internal duct flow problems in a straightforward manner following the general approach of Ref. 9.

The resulting mixed boundary value problem (Dirichlet–Neumann) for the exterior flowfield is solved by integral transform techniques. Previously, decoupling of the inflow and outflow portions of the boundary into separate Dirichlet problems was used to develop the boundary conditions for external flow problems.[2] Coupling of this global analytic solution with the nonlinear numerical solution is accomplished by the boundary conditions in an unambiguous manner. The analytic solutions provide a smooth transition across the computational boundary to the true far-field conditions at infinity. The higher-order boundary conditions are in the form of global distributions of flow quantities to be imposed along the boundary, not constant conditions. They represent a logical asymptotic extension of zero-order local conditions for external flows. The additional computational effort required to impose the higher-order boundary conditions is modest. Furthermore, the boundary analysis can be coupled with any inviscid numerical solution method. It can also be coupled with a viscous method by expressing a wake as a vorticity distribution and convecting this distribution downstream via the Euler analytic model, as demonstrated previously in Ref. 10.

Results are presented for airfoil flows, which establish the validity of the Dirichlet–Neumann analysis for the flowfield exterior to O-grid and C-grid computational boundaries. Results from baseline numerical solutions on large grids are compared with small grid results using both higher-order and zero-order conditions. Both isentropic and nonisentropic transonic airfoil flow results are presented. It is found that the far-field boundaries can be located very close to the airfoil with negligible loss in accuracy. The reduction in the number of grid points required (and computational cost) is substantial.

Analytical Formulation

The system of two-dimensional, steady, Euler equations asymptotic about a constant pressure state is presented in this section. The formulation is valid for both isentropic and nonisentropic flow conditions.

The two-dimensional form of the steady state Euler equations to be used is[11]

$$\frac{\partial\theta}{\partial x}-\frac{\partial Q}{\partial y}=-M^2\sin\theta\left[\cos\theta\frac{\partial Q}{\partial x}+\sin\theta\frac{\partial Q}{\partial y}\right]+\frac{1}{M^2}\frac{\partial S}{\partial y}$$

$$\frac{\partial\theta}{\partial y}+(1-M^2)\frac{\partial Q}{\partial x}=M^2\sin\theta\left[\cos\theta\frac{\partial Q}{\partial y}-\sin\theta\frac{\partial Q}{\partial x}\right]-\frac{1}{M^2}\frac{\partial S}{\partial x} \tag{1}$$

$$a^2+[(\gamma-1)/2]q^2=1 \tag{2}$$

The velocity magnitude and speed of sound are q and a, respectively; the flow angle is θ; and Q is the logarithm of velocity normalized by a reference velocity $\bar{q}_\infty$ defined subsequently. The local Mach number is M, and entropy S is defined in terms of pressure p and density ρ as

$$S\equiv\frac{1}{\gamma(\gamma-1)}\ln\left(\frac{p}{\rho^\gamma}\right) \tag{3}$$

The physical plane Cartesian coordinates are denoted by (x, y) and the ratio of specific heats by γ. The fact that entropy remains constant along streamlines has been incorporated into Eqs. (1).

The x axis can be aligned with the freestream direction (by rotation) without loss of generality. The asymptotic form of Eqs. (1) in the far field then becomes

$$\frac{\partial\theta}{\partial x}-\frac{\partial Q}{\partial y}=\frac{1}{M_\infty^2}\frac{\partial S_\infty}{\partial y},\qquad \frac{\partial\theta}{\partial y}+\left(1-M_\infty^2\right)\frac{\partial Q}{\partial x}=0 \tag{4}$$

For nonisentropic flow, M_∞ varies normal to the entropy wake in the downstream far field.

Using the definition (3) and the algebraic total temperature relation (2), the far-field Mach number M_∞ can be expressed as

$$M_\infty^2=\frac{2}{\gamma-1}\frac{1-\bar{a}_\infty^2\exp[(\gamma-1)S_\infty]}{\bar{a}_\infty^2\exp[(\gamma-1)S_\infty]} \tag{5}$$

The reference speed of sound, velocity, and Mach number are defined as

$$\bar{a}_\infty\equiv p_\infty^{(\gamma-1)/2\gamma},\qquad \bar{q}_\infty\equiv\sqrt{[2/(\gamma-1)]\left(1-\bar{a}_\infty^2\right)}$$

$$\bar{M}_\infty\equiv\bar{q}_\infty/\bar{a}_\infty \tag{6}$$

and are based on the assumption that the far-field pressure p_∞ is constant.

Defining a new dependent variable that includes the far-field entropy as

$$\tilde{Q}\equiv\ln\left(\sqrt{(\gamma-1)/2}q\left\{1-\bar{a}_\infty^2\exp[(\gamma-1)S_\infty]\right\}^{-\frac{1}{2}}\right) \tag{7}$$

then Eqs. (1) become

$$\frac{\partial\theta}{\partial x}-\frac{\partial\tilde{Q}}{\partial y}=R_1,\qquad \frac{\partial\theta}{\partial y}+\beta^2\frac{\partial\tilde{Q}}{\partial x}=R_2 \tag{8}$$

where

$$\beta^2\equiv 1-\bar{M}_\infty^2 \tag{9}$$

For isentropic flow, Q and $\tilde{Q}$ are identical and $\bar{q}_\infty$ is the global freestream velocity. The RHS terms R_1 and R_2 are defined as

$$R_1\equiv -M^2\sin\theta\left[\cos\theta\frac{\partial Q}{\partial x}+\sin\theta\frac{\partial Q}{\partial y}\right]+\frac{1}{M^2}\frac{\partial S}{\partial y}-\frac{1}{M_\infty^2}\frac{\partial S_\infty}{\partial y} \tag{10}$$

$$R_2=M^2\sin\theta\left[\cos\theta\frac{\partial Q}{\partial y}-\sin\theta\frac{\partial Q}{\partial x}\right]$$

$$+\left(M^2-\bar{M}_\infty^2\right)\frac{\partial Q}{\partial x}-\frac{1}{M^2}\frac{\partial S}{\partial x} \tag{11}$$

Both R_1 and R_2 vanish in the far field along with the dependent variables θ and $\tilde{Q}$.

A higher-order description of the flowfield behavior at and beyond the computational boundary can be obtained by neglecting the RHS terms R_1 and R_2 and solving the resulting homogeneous equations. The exact solution, however, can be obtained if necessary by asymptotic iterative correction because R_1 and R_2 are small and well-behaved in the region exterior to the boundary. This approach was demonstrated in Ref. 12.

Solution of Homogeneous Equations

The homogeneous subset of Eqs. (8) provides a higher-order model of the flowfield beyond the computational boundary. The numerical solution inside the boundary propagates information of a different type to the inflow and outflow portions of the boundary, as described in Ref. 2. This differing information (Dirichlet–Neumann) serves as boundary conditions for Eqs. (8). The procedure for solution of the homogeneous mixed boundary value problem, including the necessary mappings, is presented in this section.

The Prandtl–Glauert scaling transformation defined by

$$\tilde{x}\equiv x,\qquad \tilde{y}\equiv\beta y,\qquad \tilde{\theta}=\theta/\beta \tag{12}$$

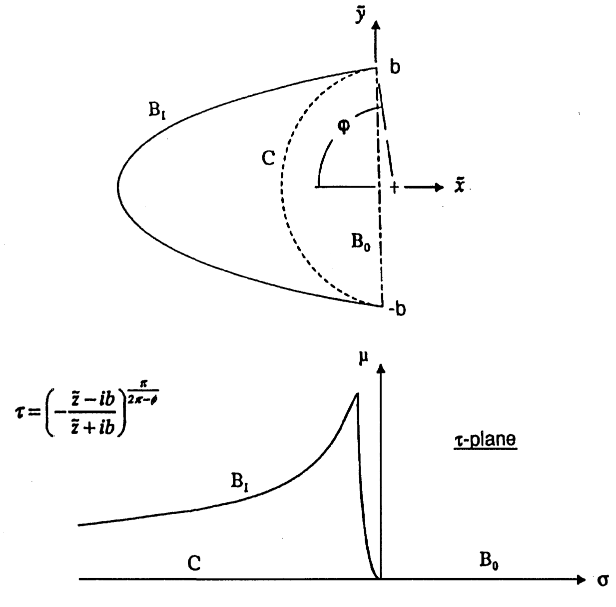

Fig. 1 Mapping of downstream boundary and circular arc to the real axis.

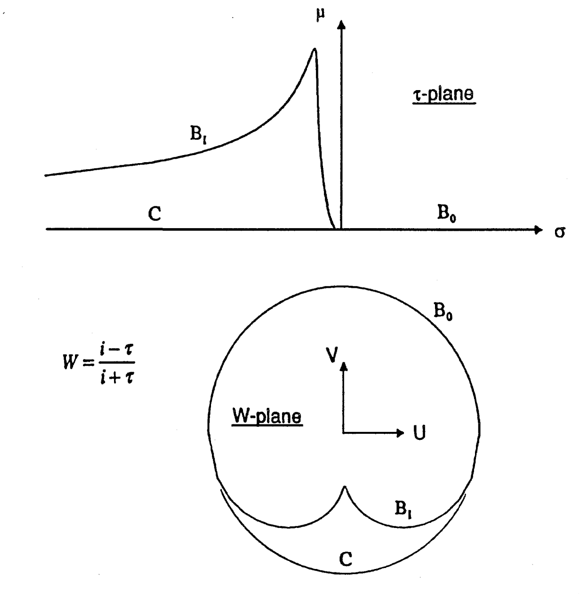

Fig. 2 Mapping of real axis to a circle (boundary to cusped circle).

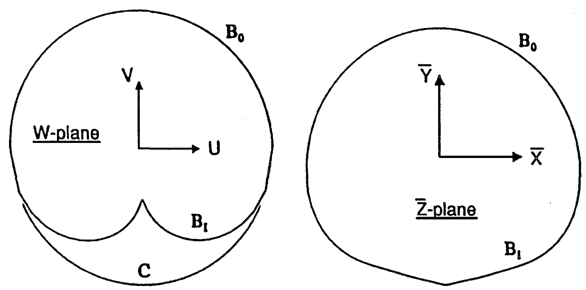

Fig. 3 Mapping of computational boundary to nearly circular shape, $\bar{Z} = \sqrt{[(W + ic)^2 + d^2]}$.

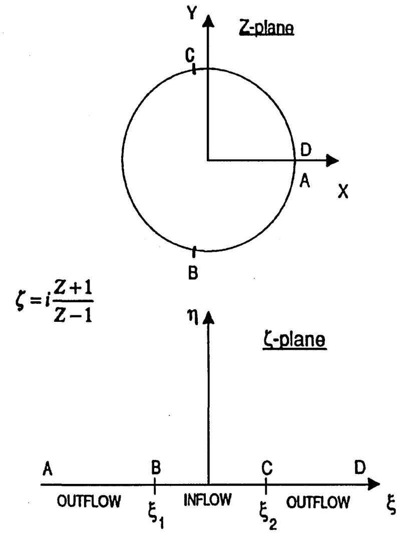

Fig. 4 Computational boundary mapping to the real axis.

transforms the homogeneous subset of Eqs. (8) into the Cauchy–Riemann form

$$\frac{\partial\tilde{\theta}}{\partial\bar{x}} - \frac{\partial\tilde{Q}}{\partial\bar{y}} = 0, \qquad \frac{\partial\tilde{\theta}}{\partial\bar{y}} + \frac{\partial\tilde{Q}}{\partial\bar{x}} = 0 \tag{13}$$

For a C-grid topology, a sequence of mappings can be applied to the boundary shape that conformally maps it to a circle and preserves the Cauchy–Riemann form of the far-field model (13) in the circle plane. The circular arc mapping

$$\tau = \left(-\frac{\bar{z} - ib}{\bar{z} + ib}\right)^{\pi/(2\pi-\phi)}, \qquad \tau \equiv \sigma + i\mu \tag{14}$$

where $\bar{z} = \bar{x} + i\bar{y}$ maps the downstream outflow boundary B_o and an inscribed circular arc C to the real axis, as shown in Fig. 1. The arc C is tangent to the inflow boundary B_I at the corner points $\bar{z} = \pm ib$ as shown. The linear fractional transformation

$$W = (i - \tau)/(i + \tau), \qquad W \equiv U + iV \tag{15}$$

maps the real axis onto the perimeter of a circle and the far-field region to its interior. The image of the inflow boundary B_I has a cusped-like shape, as shown in Fig. 2. The cusp can be removed by the Schwarz–Christoffel mapping

$$\bar{Z} = \sqrt{(W + ic)^2 + d^2}, \qquad \bar{Z} \equiv \bar{X} + i\bar{Y} \tag{16}$$

The two parameters c and d can be adjusted to make the boundary image nearly circular, as shown in Fig. 3. Finally, the Fourier mapping

$$\bar{Z} = Z + A_0 \log Z + \sum_{k=1}^{\infty} A_k Z^{-k}, \qquad Z = X + iY \tag{17}$$

maps the near-circular image to the unit circle. The mapping (17) can also be applied to an O-grid topology to map the boundary to the unit circle. Additional details are given in Ref. 13. At this point the analysis for the two types of topology proceeds in the same manner.

The unit circle is mapped to the real axis by the linear fractional transformation

$$\zeta = i[(Z + 1)/(Z - 1)], \qquad \zeta \equiv \xi + i\eta \tag{18}$$

The exterior flowfield is mapped to the upper half-plane. The inflow portion of the boundary lies between ξ_1 and ξ_2, as shown in Fig. 4. The upper-half of the ζ plane is mapped to the interior of an infinite strip by the logarithmic transformation

$$w = \tfrac{1}{2}\log[(\zeta - \xi_2)/(\zeta - \xi_1)], \qquad w \equiv u + iv \tag{19}$$

The upper boundary of the strip is the image of the inflow portion of the computational boundary, whereas the lower boundary corresponds to the outflow portion, as shown in Fig. 5.

The flow crossing the inflow portion of the computational boundary from upstream can be assumed isentropic so that the information propagated to this portion of the boundary by the numerical solution can be represented by

$$\tilde{Q}_b = \ln(q_b/\bar{q}_\infty) \tag{20}$$

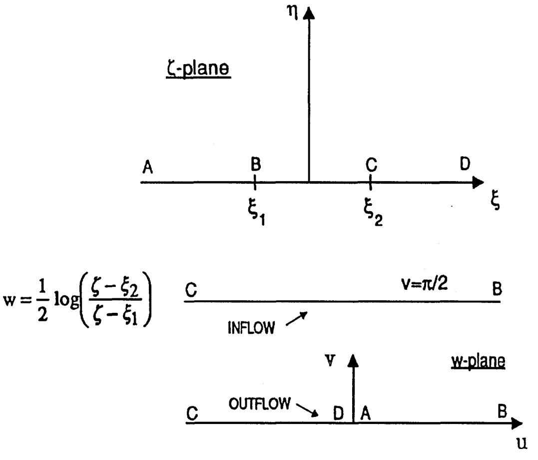

Fig. 5 Upper half-plane mapping to an infinite strip.

Numerical solution information propagated upstream to the computational boundary is typically in the form of the Riemann variable $q-2a/(\gamma-1)$. Using the total temperature relation (2), this quantity can be expressed in terms of boundary velocity q_b, and subsequently $\tilde{Q}_b$, in a straightforward manner. Likewise, information propagated by the numerical solution to the outflow portion of the boundary can be represented by

$$\tilde{\theta}_b = \theta_b/\beta \tag{21}$$

Numerical solution boundary values are denoted by q_b and θ_b. This information provides the boundary data for the far-field analytic model. A more thorough explanation is provided in Ref. 2.

The conformal mappings (14–19) preserve the Cauchy–Riemann form of the governing equations, and their solution in the w-plane can be obtained using Fourier integral transforms. The solution for $\tilde{Q}$ and $\tilde{\theta}$ is

$$\begin{aligned}\tilde{Q} = {} & \frac{1}{\pi}\int_{-\infty}^{\infty}\frac{\tilde{Q}_b(\sigma)\cosh(\sigma-u)\cos v\,\mathrm{d}\sigma}{\sinh^2(\sigma-u)+\cos^2 v} \\ & - \frac{1}{\pi}\int_{-\infty}^{\infty}\frac{\tilde{\theta}_b(\sigma)\sinh(\sigma-u)\cos v\,\mathrm{d}\sigma}{\sinh^2(\sigma-u)+\sin^2 v}\end{aligned} \tag{22}$$

$$\begin{aligned}\tilde{\theta} = {} & \frac{1}{\pi}\int_{-\infty}^{\infty}\frac{\tilde{\theta}_b(\sigma)\cosh(\sigma-u)\sin v\,\mathrm{d}\sigma}{\sinh^2(\sigma-u)+\sin^2 v} \\ & - \frac{1}{\pi}\int_{-\infty}^{\infty}\frac{\tilde{Q}_b(\sigma)\sinh(\sigma-u)\sin v\,\mathrm{d}\sigma}{\sinh^2(\sigma-u)+\cos^2 v}\end{aligned} \tag{23}$$

The coordinates (u, v) represent the image of points in the physical plane exterior to and including the boundary. Along the inflow boundary,

$$\tilde{Q} = \frac{1}{\pi}\lim_{\varepsilon\to 0}\int_{-\infty}^{\infty}\frac{\tilde{Q}_b(\sigma)\cosh(\sigma-u)\varepsilon\,\mathrm{d}\sigma}{\sinh^2(\sigma-u)+\varepsilon^2} = \tilde{Q}_b(u) \tag{24}$$

$$\tilde{\theta} = \frac{1}{\pi}\int_{-\infty}^{\infty}\frac{\tilde{\theta}_b(\sigma)\,\mathrm{d}\sigma}{\cosh(\sigma-u)} - \frac{1}{\pi}\lim_{\varepsilon\to 0}\int_{-\infty}^{\infty}\frac{\tilde{Q}_b(\sigma)\sinh(\sigma-u)\,\mathrm{d}\sigma}{\sinh^2(\sigma-u)+\varepsilon^2} \tag{25}$$

Along the outflow boundary,

$$\tilde{\theta} = \frac{1}{\pi}\lim_{\varepsilon\to 0}\int_{-\infty}^{\infty}\frac{\tilde{\theta}_b(\sigma)\cosh(\sigma-u)\varepsilon\,\mathrm{d}\sigma}{\sinh^2(\sigma-u)+\varepsilon^2} = \tilde{\theta}_b(u) \tag{26}$$

$$\tilde{Q} = \frac{1}{\pi}\int_{-\infty}^{\infty}\frac{\tilde{Q}_b(\sigma)\,\mathrm{d}\sigma}{\cosh(\sigma-u)} - \frac{1}{\pi}\lim_{\varepsilon\to 0}\int_{-\infty}^{\infty}\frac{\tilde{\theta}_b(\sigma)\sinh(\sigma-u)\,\mathrm{d}\sigma}{\sinh^2(\sigma-u)+\varepsilon^2} \tag{27}$$

Development of Boundary Conditions

At a subsonic far-field computational boundary, there are three downstream-running waves and one upstream-running wave. Therefore, the information available from the numerical solution is not complete and differs at the inflow and outflow boundaries. The information lacking must be provided by the boundary conditions. If the flow is supersonic, all waves are downstream running and specification of boundary conditions is straightforward.

Far-field computational boundary conditions (subsonic) are developed in this section based on the solution of the higher-order Euler model obtained in the preceding section. This solution is assumed valid in the region beyond the computational boundary where nonlinear effects are not large. Within the computational boundaries, the full nonlinear Euler equations must be solved numerically. The boundary conditions provide for a smooth coupling of the nonlinear and far-field solutions so that the true conditions at infinity can be imposed.

Inflow Boundary

Along the inflow portion of the boundary (isentropic conditions assumed), there are two downstream-running waves propagating information to the boundary from outside the computational domain, i.e., from upstream infinity, and one upstream-running wave propagating information from the numerical solution.[2] The incoming information is represented by the Riemann variable $q+2a/(\gamma-1)$ and the flow angle θ. The outgoing information is represented by the Riemann variable $q-2a/(\gamma-1)$. The solution (23) provides one of the lacking information elements from outside the computational domain; the remaining information is provided by the total temperature relation (2).

The numerical solution propagates to the boundary the Riemann variable $q-2a/(\gamma-1)$, which can be converted to q_b (and $\tilde{Q}_b$) as explained earlier. Using the total temperature relation the boundary distribution of the downstream-propagating Riemann variable, i.e., the boundary conditions, is calculated according to

$$\left(q+\frac{2}{\gamma-1}a\right)_{\mathrm{bc}} = q_b + \frac{2}{\gamma-1}\sqrt{1-\frac{\gamma-1}{2}q_b^2} \tag{28}$$

The distribution of flow angle on the inflow portion of the computational boundary in the airfoil frame of reference is provided by the solution (25) as

$$\begin{aligned}\theta_{\mathrm{bc}} = {} & \theta_\infty + \frac{\beta}{\pi}\int_{-\infty}^{\infty}\frac{\tilde{\theta}_b(\sigma)\,\mathrm{d}\sigma}{\cosh(\sigma-u)} \\ & - \frac{\beta}{\pi}\lim_{\varepsilon\to 0}\int_{-\infty}^{\infty}\frac{\tilde{Q}_b(\sigma)\sinh(\sigma-u)\,\mathrm{d}\sigma}{\sinh^2(\sigma-u)+\varepsilon^2}\end{aligned} \tag{29}$$

The quantity u represents the image of a computational boundary point in physical space, and θ_∞ is related to the airfoil angle of attack. Within the first integral $\tilde{\theta}_b$ represents the information propagated to the outflow portion of the boundary by the numerical solution whereas $\tilde{Q}_b$ in the second integral represents velocity information propagated to the inflow portion, as already explained. The expression (25) is obtained from the solution (23) in the limit as v approaches $\pi/2$ and represents a quadrature along the boundary.

Zero-order (or characteristic) boundary conditions would consist of imposing the constant values $\bar{q}_\infty + 2\bar{a}_\infty/(\gamma-1)$ and $\theta_\infty = \mathrm{const}$ along the inflow portion of the boundary.

Outflow Boundary

Along the outflow portion of the boundary there are three (two for isentropic conditions) downstream-running waves propagating information to the boundary from the numerical solution and one upstream-running wave propagating information from outside the computational domain, i.e., from downstream infinity. The solution (22) provides the lacking information from outside the computational domain.

In the limit as v approaches zero, the solution (22) reduces to Eq. (27). As in Eq. (29), $\tilde{\theta}_b$ and $\tilde{Q}_b$ represent numerical solution

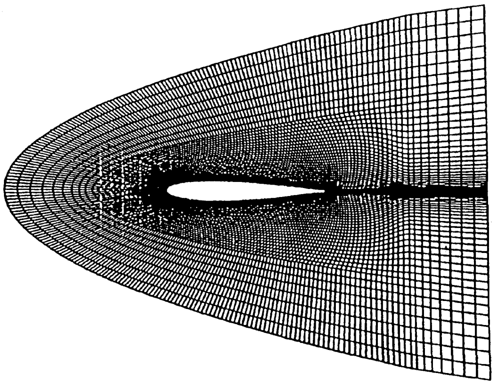

Fig. 6 Core grid for NACA 0012 airfoil.

information propagated to the outflow and inflow portions of the boundary, respectively. From definition (7), the velocity distribution along the outflow portion of the boundary obtained from the analytic solution is

$$q = \sqrt{2/(\gamma - 1)}\left\{1 - \bar{a}_\infty^2 \exp[(\gamma - 1)S_\infty]\right\}^{\frac{1}{2}} e^{\tilde{Q}} \tag{30}$$

where $\tilde{Q}$ is obtained by quadrature from relation (27). The quantity S_∞ can be approximated by numerical solution values of S at the boundary for nonisentropic conditions. This approximation neglects streamline curvature downstream of the boundary. Using the total temperature relation (2), the boundary distribution of the upstream propagating Riemann variable, i.e., the boundary conditions, is calculated according to

$$\left(q - \frac{2}{\gamma - 1}a\right)_{\mathrm{bc}} = \left(q + \frac{2}{\gamma - 1}a\right)_{\mathrm{num}} - \frac{4}{\gamma - 1}\sqrt{1 - \frac{\gamma - 1}{2}q^2} \tag{31}$$

The value of q under the radical is obtained from Eq. (30), and the remaining RHS term represents information propagated to the boundary by the numerical solution. This formulation uses the analytic solution to describe the pressure field exterior to the outflow boundary.

Conventional practice using zero-order boundary conditions would consist of imposing the constant value $\bar{q}_\infty - 2\bar{a}_\infty/(\gamma - 1)$ along the outflow portion of the boundary.

Results and Discussion

The boundary condition procedures just developed have been implemented successfully in the two-dimensional Euler computational fluid dynamics (CFD) codes FLO672D (Ref. 14) and CFL2D (Ref. 15). Results for the NACA 0012 airfoil are presented for both subsonic and transonic conditions.

Global boundary condition models for subsonic external flows lead to mixed boundary value problems. The procedure developed for the solution of such problems was validated in Ref. 16 by means of the exact solution for incompressible flow past a circular cylinder. A circular boundary was located asymmetrically around the cylinder and mixed information typical of a numerical solution was placed on the boundary from the exact solution. The exterior analysis was used to provide the missing boundary information, which was then compared to the exact values from the cylinder solution. The results were nearly identical (within numerical quadrature error) to those taken from the exact cylinder solution.

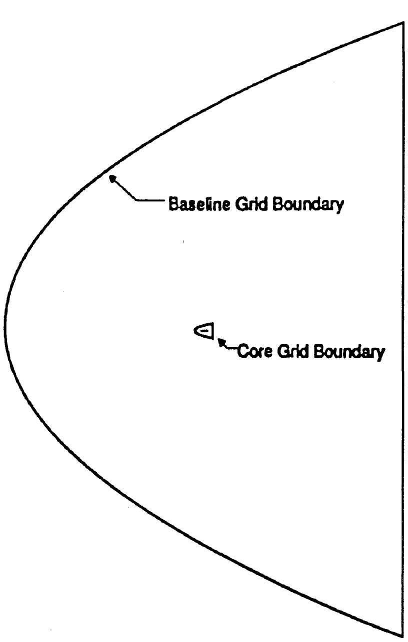

Fig. 7 Relative boundary locations of baseline and core grids.

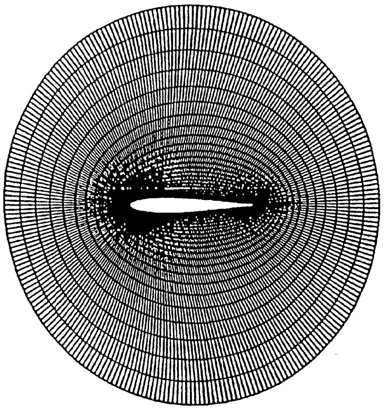

Fig. 8 Core grid for NACA 0012 airfoil.

To demonstrate the higher-order boundary condition implementation, baseline results for the NACA 0012 airfoil were calculated using FLO672D on a large C-grid and a large O-grid whose far-field boundaries were located approximately 40 chord lengths from the airfoil. This distance was sufficiently large that the zero-order (characteristic) and higher-order boundary conditions produced almost identical numerical flowfield predictions. The calculations were repeated on a much smaller C-grid and O-grid using both the zero-order and first-order boundary conditions. The small-grid boundaries were very close to the airfoil (approximately one chord). These small-grid results are compared with the baseline results from the large grid to assess the higher-order boundary condition accuracy.

The small core C-grid shown in Fig. 6 had 241 points in the circumferential direction and 41 points in the radial direction, with 177 points on the airfoil surface. The large baseline grid had dimensions 305 × 73 and was constructed by simply adding parabolic C-lines outside the core grid inflow boundary and vertical lines downstream of the outflow boundary. The relative locations of the outer boundaries of the two C-grids are shown in Fig. 7. The core O-grid shown in Fig. 8 had 256 points in the circumferential direction and 24 points in the radial direction. Both core grids extended one chord length upstream of the airfoil leading edge and one chord length downstream of the trailing edge. They remained unchanged for all of the calculations. The large baseline O-grid had dimensions 256 × 64 and was constructed by simply adding concentric circles and radial lines beyond the core grid boundary. Both baseline grids extended approximately 40 chord lengths upstream and downstream of the airfoil. The relative locations of the outer boundaries of the two O-grids are shown in Fig. 9.

Surface pressures predicted by the FLO672D code using the core grids of Figs. 6 and 8 are presented in Fig. 10. The freestream Mach number was 0.40, and the angle of attack was 8 deg. Results for both zero-order and higher-order global boundary conditions are shown along with baseline results from the large grids. The higher-order boundary conditions produced results nearly identical to the baseline results, whereas the zero-order boundary conditions produced considerable solution degradation.

Transonic results are shown in Figs. 11 (nonlifting) and 12 (lifting). The freestream Mach number was 0.85, and the angle of attack

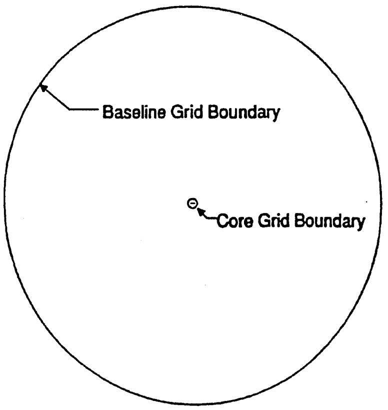

Fig. 9 Relative boundary locations of baseline and core grids.

was zero for the nonlifting case. For the lifting case, the Mach number was 0.80 and the angle of attack was 2 deg. The higher-order boundary conditions again produced results nearly identical to the baseline results. However, the baseline results are slightly different near the shock wave location for the two grid topologies. The most noticeable effect of the zero-order boundary conditions is the incorrect prediction of the shock location and strength. Pressure contours for the lifting case are shown in Figs. 13 and 14.

Results obtained using the CFL2D code and the C-grid are shown in Figs. 15 and 16. Inviscid surface pressure comparisons in Fig. 15 show that the higher-order boundary conditions produce results nearly identical to the baseline results. Pressure contours are shown in Fig. 16.

Overall consistency of the global boundary condition procedure is demonstrated by the transonic Mach number contours shown in Fig. 17 for the NACA 0012 airfoil. The freestream Mach number was 0.80 and the angle of attack was 2 deg. Near-field contours from

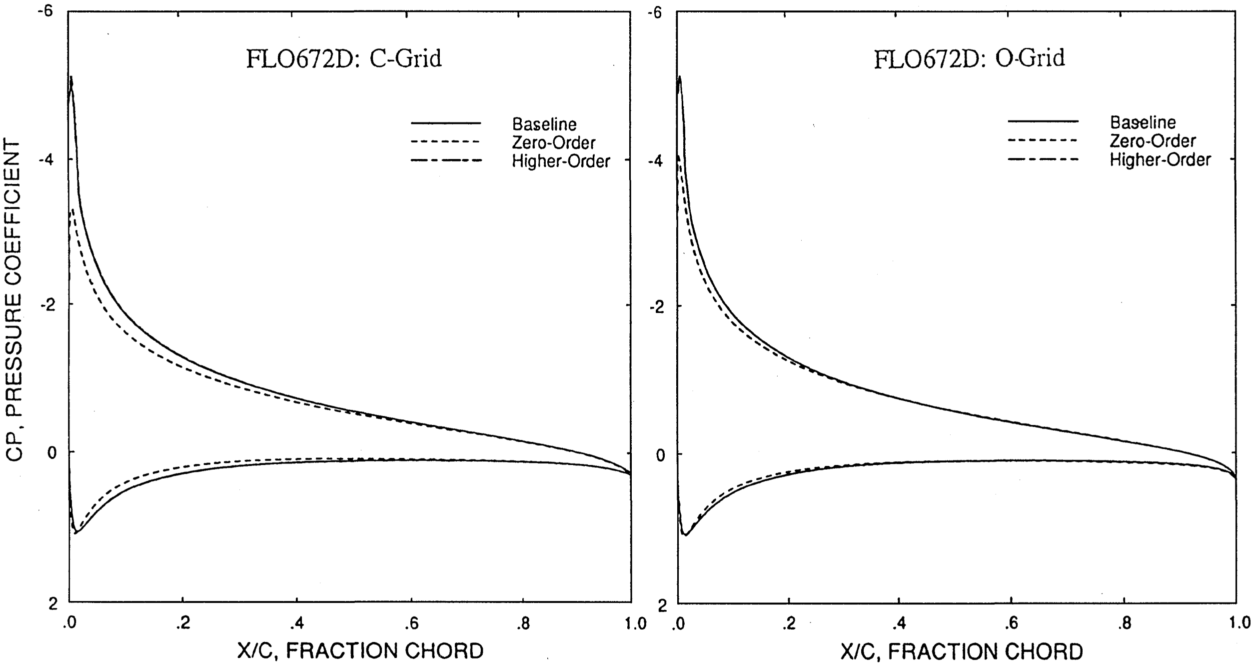

Fig. 10 Surface pressure predictions using zero- and higher-order boundary conditions, M_∞ = 0.40 and α = 8 deg.

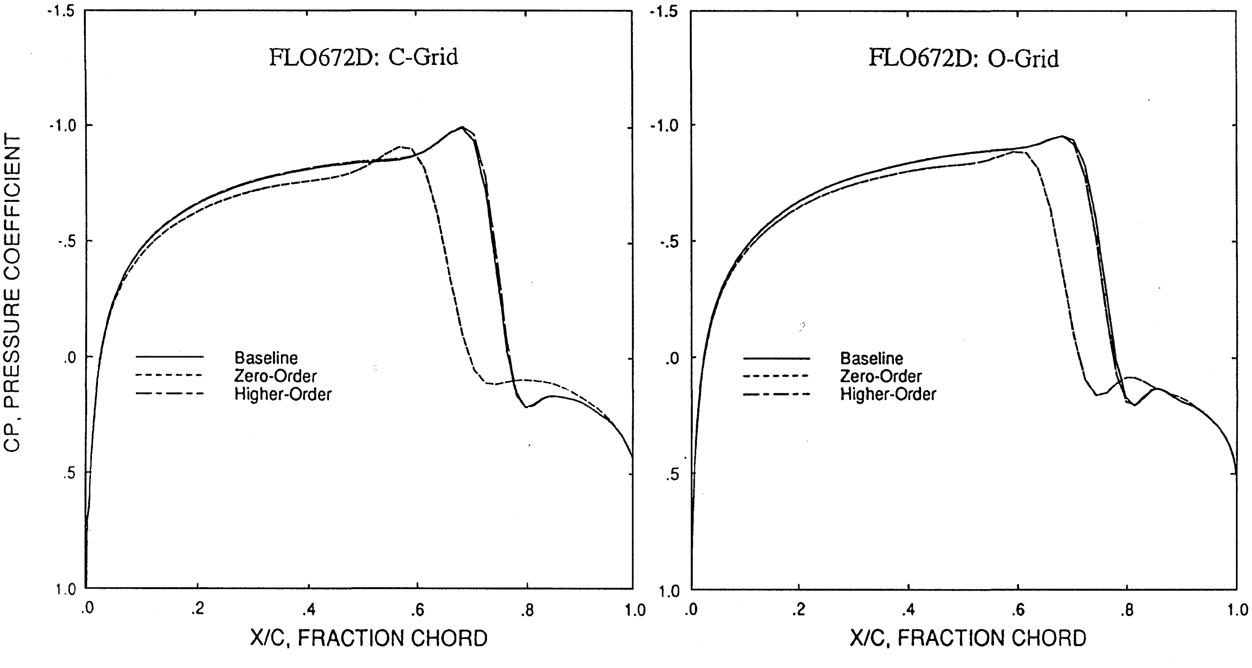

Fig. 11 Surface pressure predictions using zero- and higher-order boundary conditions, M_∞ = 0.85 and α = 0 deg.

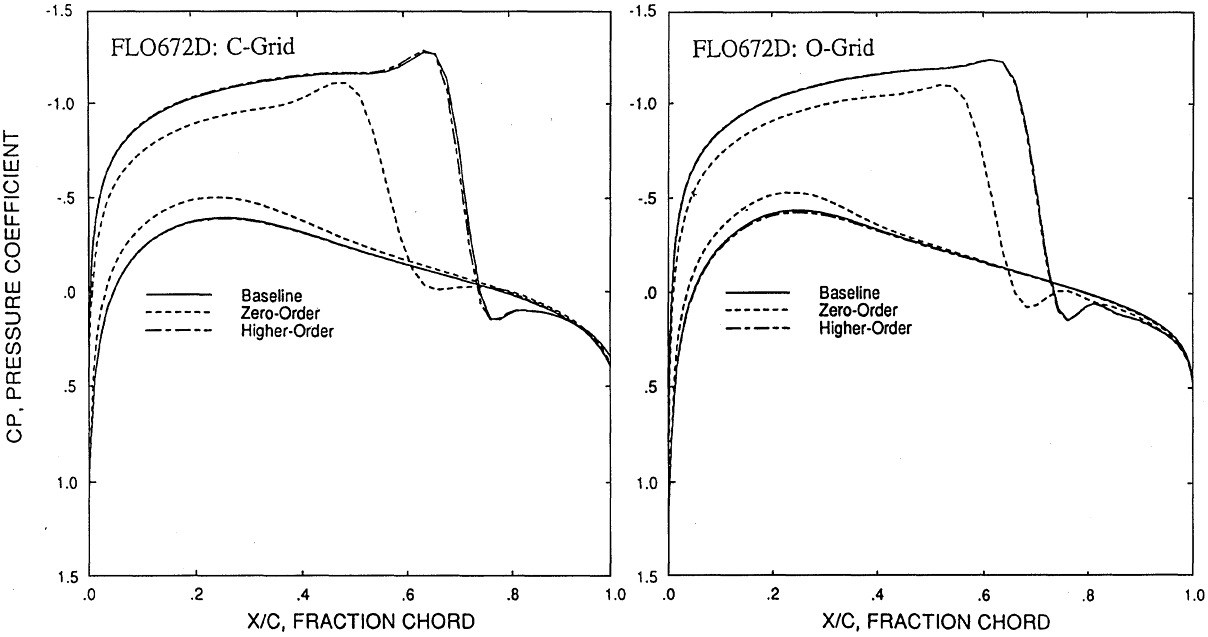

Fig. 12 Surface pressure predictions using zero- and higher-order boundary conditions, $M_\infty = 0.80$ and $\alpha = 2$ deg.

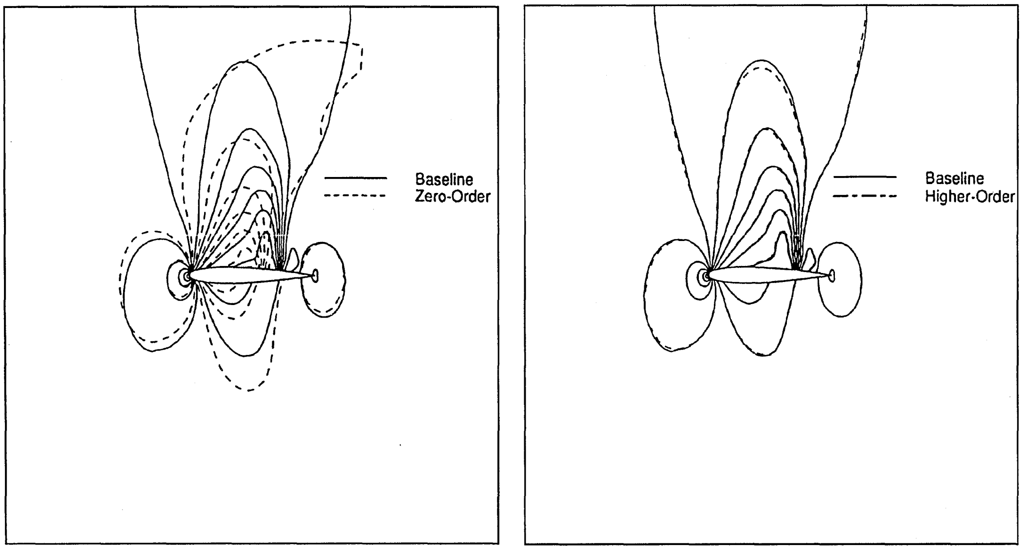

Fig. 13 Pressure contours predicted using zero- and higher-order boundary conditions, C-grid, FLO672D; $M_\infty = 0.80$ and $\alpha = 2$ deg.

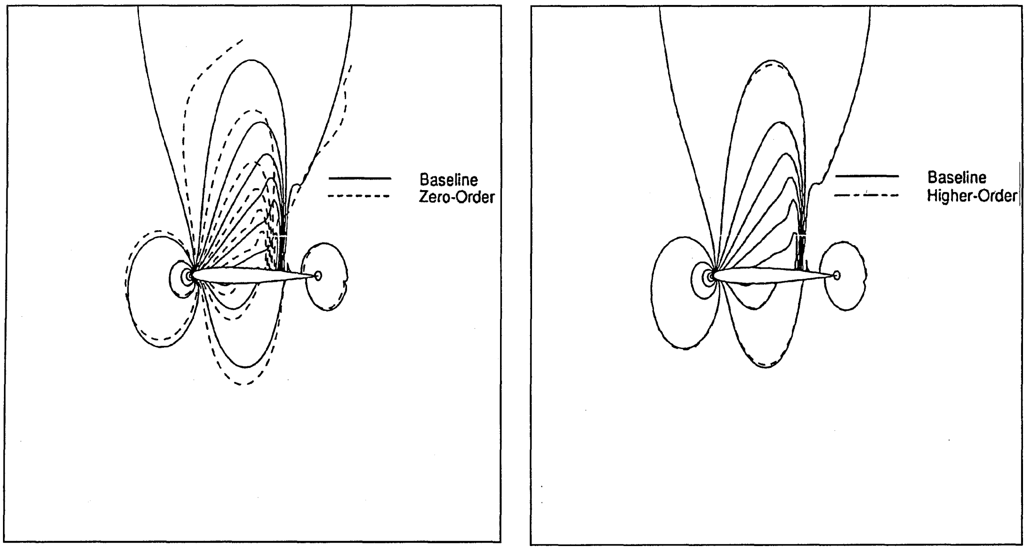

Fig. 14 Pressure contours predicted using zero- and higher-order boundary conditions, O-grid, FLO672D; $M_\infty = 0.80$ and $\alpha = 2$ deg.

the FLO672D computation on the small grid match smoothly with the far-field contours from the analytic solution, including the nonisentropic portion of the field. The computational boundary shape was elliptic to simplify the calculation of the far-field analytic solution and its contours. The boundary was situated approximately one chord length above the airfoil to lie outside of the embedded supersonic region on the upper surface.

Large efficiency gains can be achieved by incorporating more accurate far-field boundary conditions into numerical flowfield solution methods. The number of computational grid points for a given accuracy level was reduced by approximately 60% by using higher-order conditions. The reduction is potentially greater for three-dimensional applications. Only a modest increase in computational effort (approximately 2%) is required for the higher-order conditions. An additional efficiency gain is also provided in that fewer iterations are typically required for solution convergence because of the closer proximity of the far-field boundaries. These gains have not been quantified precisely because no attempt has yet been made to optimize the implementation with any particular numerical solution algorithm.

The present approach of replacing the intermediate- and far-field portions of the flowfield with an analytic model is being extended to three dimensions. Initial application is to a grid topology having planar boundaries. Details can be found in Ref. 17.

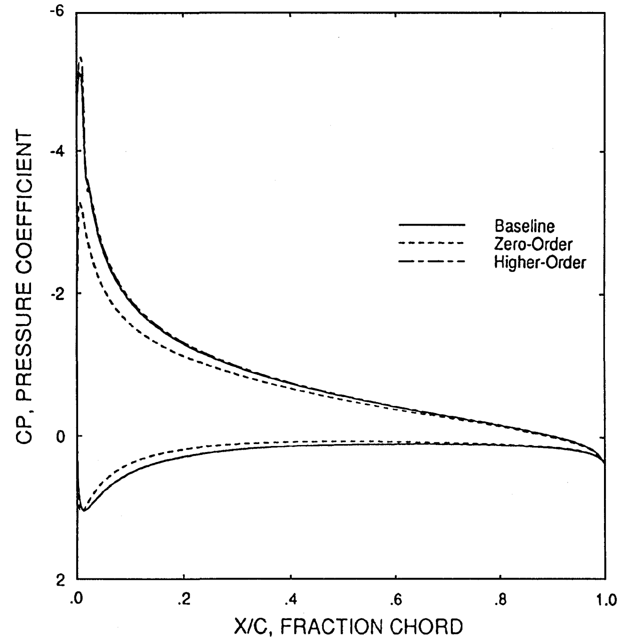

Fig. 15 Surface pressure predictions using zero- and higher-order boundary conditions, C-grid, CFL2D; $M_\infty = 0.40$ and $\alpha = 8$ deg.

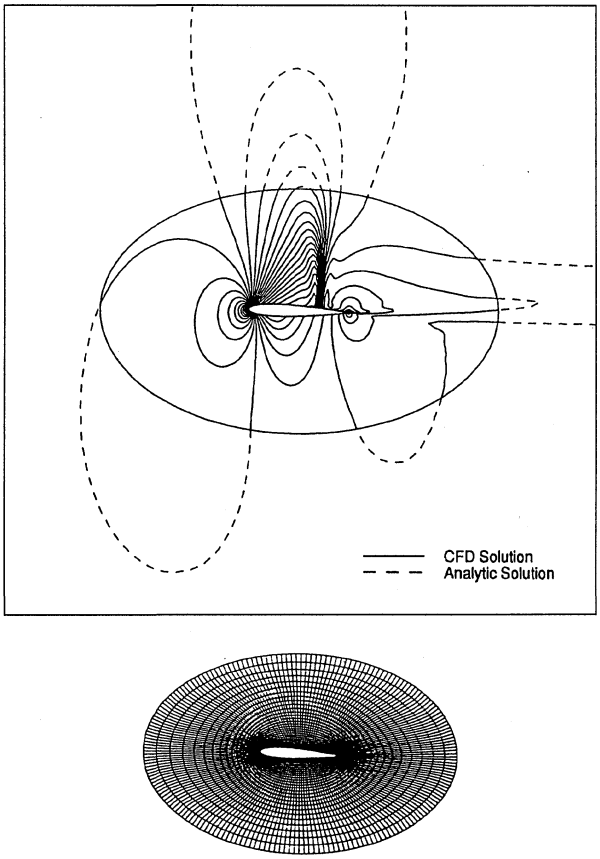

Fig. 17 Transonic Mach number contours with far-field analytic solution added, FLO672D; $M_\infty = 0.80$ and $\alpha = 2$ deg.

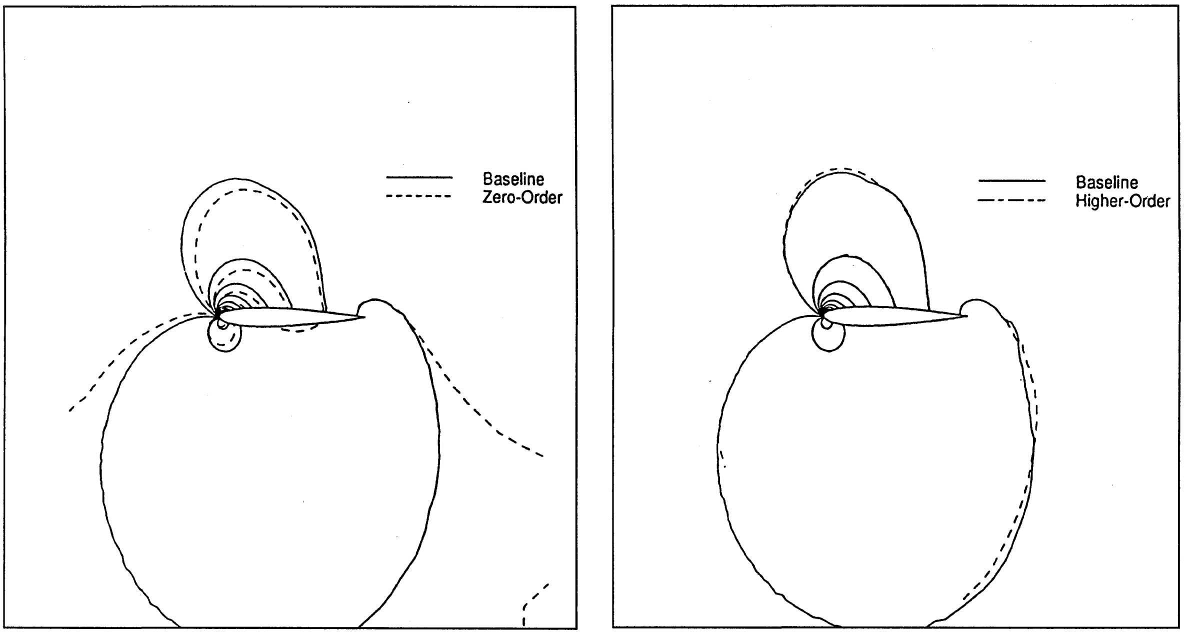

Fig. 16 Pressure contours predicted using zero- and higher-order boundary conditions, C-grid, CFL2D; $M_\infty = 0.40$ and $\alpha = 8$ deg.

Summary

Far-field computational boundary conditions for C-grid and O-grid topologies have been developed for two-dimensional external flow problems. Improvements in the analytic formulation over previous work are included. These global higher-order boundary conditions are derived from analytic solutions of an asymptotic form of the Euler equations and represent a logical extension of the zero-order (or characteristic) local boundary conditions commonly used in the numerical solution of nonlinear fluid dynamic equations. Transformations are introduced that lead to linear equations to be solved in the far field, but the fluid dynamic variables are not linearized and small perturbations are not assumed.

The boundary conditions and analytic solutions provide a smooth transition across a computational boundary to the true far-field conditions at infinity. The boundary procedure is general in that it can be used in conjunction with any inviscid numerical solution method and either C-grid or O-grid topologies.

The higher-order boundary conditions allow the far-field boundaries to be located much closer, thereby reducing the number of grid points needed for the numerical solution and also the number of iterations for solution convergence. This allows a significant reduction in the amount of computational effort required for the nonlinear numerical solution because the additional calculations required for the higher-order boundary conditions is modest. Results were shown where the number of grid points was reduced by approximately 60%.

Because the boundary conditions are derived from the Euler equations, the flow crossing the boundaries can be rotational (nonisentropic) and they can be used for calculating transonic flows containing shock waves. Previous work used a linearization of the thermodynamic relations in developing the nonisentropic boundary condition model. That restriction has been removed by the present analysis. It also provides a procedure for global solution of the exterior flowfield by solving the associated mixed boundary value problem. Earlier work had partitioned the exterior field into two Dirichlet problems defined by the respective inflow and outflow conditions along the computational boundary.

Representing the vorticity distribution of a viscous wake as an entropy distribution and allowing this wake to convect downstream undamped allows the boundary conditions procedure to be used with Navier–Stokes codes for viscous calculations. This viscous flow application is only an approximation, because the Euler analytic far-field model preserves a vorticity wake to infinity, whereas a viscous wake eventually decays.

Acknowledgments

This research was partially supported by the McDonnell Douglas Independent Research and Development Program and partially by the U.S. Air Force under Contract F33615-94-C-3000 (Don W. Kinsey, Program Manager). The author would like to thank Michael McDevitt for his assistance in carrying out the calculations.

References

[1] Verhoff, A., and Stookesberry, D., "Second-Order, Far-Field Computational Boundary Conditions for Inviscid Duct Flow Problems," *AIAA Journal*, Vol. 30, No. 5, 1992, pp. 1268–1276.

[2] Verhoff, A., Stookesberry, D., and Agrawal, S., "Far-Field Computational Boundary Conditions for Two-Dimensional External Flow Problems," *AIAA Journal*, Vol. 30, No. 11, 1992, pp. 2585–2594.

[3] Engquist, B., and Majda, A., "Absorbing Boundary Conditions for the Numerical Simulation of Waves," *Mathematics of Computation*, Vol. 31, No. 139, 1977, pp. 629–651.

[4] Higdon, R. L., "Initial-Boundary Value Problems for Linear Hyperbolic Systems," *SIAM Review*, Vol. 28, No. 2, 1986, pp. 177–217.

[5] Giles, M. B., "Nonreflecting Boundary Conditions for Euler Equation Calculations," *AIAA Journal*, Vol. 28, No. 12, 1990, pp. 2050–2058.

[6] Hirsch, C., and Verhoff, A., "Far-Field Numerical Boundary Conditions for Internal and Cascade Flow Computations," AIAA Paper 89-1943, June 1989.

[7] Ferm, L., "Open Boundary Conditions for Stationary Inviscid Flow Problems," *Journal of Computational Physics*, Vol. 78, No. 1, 1988, pp. 94–113.

[8] Ferm, L., "Open Boundary Conditions for External Flow Problems," *Journal of Computational Physics*, Vol. 91, No. 1, 1990, pp. 55–70.

[9] Verhoff, A., and Stookesberry, D., "Far-Field Computational Boundary Conditions for Internal Flow Problems," U.S. Naval Postgraduate School, NPS67-88-001CR, Monterey, CA, Sept. 1988.

[10] Verhoff, A., Stookesberry, D., and Agrawal, S., "Far-Field Computational Boundary Conditions for Transonic Flows," 4th International Symposium on Computational Fluid Dynamics, Univ. of California, Davis, CA, Sept. 1991.

[11] Verhoff, A., Stookesberry, D., and Michal, T., "Transonic Euler Solutions for Airfoils Using Asymptotic Iterative Corrections: Analysis," AIAA Paper 94-2198, June 1994.

[12] Verhoff, A., and Stookesberry, D., "Solution of the Euler Equations for Airfoils Using Asymptotic Methods," AIAA Paper 93-2931, July 1993.

[13] Halsey, N. D., "Potential Flow Analysis of Multielement Airfoils Using Conformal Mapping," AIAA Paper 79-0271, Jan. 1979.

[14] Jameson, A., "A Vertex Based Multigrid Algorithm for Three-Dimensional Flow Calculations," Vol. 78, Applied Mechanics Div., American Society of Mechanical Engineers, New York, 1986, pp. 45–73.

[15] Rumsey, C. L., Taylor, S., Thomas, J. L., and Anderson, W. K., "Application of an Upwind Navier–Stokes Code to Two-Dimensional Transonic Airfoil Flow," AIAA Paper 87-0413, Jan. 1987.

[16] Verhoff, A., "First-Order Far-Field Computational Boundary Conditions for O-Grid Topologies," AIAA Paper 95-0563, Jan. 1995.

[17] Verhoff, A., "Far-Field Computational Boundary Conditions for Three-Dimensional External Flow Problems," AIAA Paper 96-0892, Jan. 1996.

D. S. McRae
Associate Editor